Experimental evaluation of predicted undrained pore pressure generation as function of stress path and orientation in the Draupne shale

M. Soldal[1,2], J. C. Choi[2], and E. Skurtveit[2]

[1] Department of Geosciences, University of Oslo, Oslo 0371, Norway

[2] NGI – Norwegian Geotechnical Institute, Oslo 0806, Norway

Corresponding author: Magnus Soldal (magnus.soldal@ngi.no)

Key Points:

- Effects of stress path and orientation on pore pressure generation are predicted from theory and minimal experimental data
- The predictions are compared to measurements made in a series of undrained, triaxial tests on the North Sea Draupne Formation shale
- Results show that pore pressure can be accurately predicted using a combination of Skempton's formulation and anisotropic poroelasticity

Abstract

Injection or production of fluids from subsurface reservoirs lead to stress changes affecting both reservoir and surrounding rocks. For low-permeable caprocks overlying such reservoirs, the movement of pore fluids to or from the formation is restricted and the immediate and short-term response to changes in the stress field will be undrained. Consequently, stress changes transfer partly into pore pressure changes. The aim of the current study is to investigate theoretical means of forecasting the undrained pore pressure generation in the Draupne Formation shale and to compare predictions with experimental results. Predictions are based on measurements from a single undrained triaxial test on a sample with known orientation, and a combination of Skempton's classical formulation and anisotropic poroelastic theory. The predicted pore pressures are compared to measured pore pressures from a series of triaxial tests on samples with various orientations exposed to different total stress paths. First, it is confirmed that the normalized undrained pore pressure measured is linearly connected to the total stress path. Then it is demonstrated that a tensorial pore pressure parameter can be used to accurately predict the influence of stress orientation on generated pore pressure. Lastly, it is experimentally confirmed that the two predictions can be combined to predict the pore pressure arising from stress changes along any compressional stress path and orientation. The observations herein may contribute significantly to the understanding of induced pore pressure in low-permeable materials and provide valuable input to geomechanical modeling of various field operations.

Plain Language Summary

Fluid production from or injection into geological reservoirs usually cause changes in stresses experienced by both reservoir and surrounding rocks. In the low-permeable caprocks found above reservoirs, fluids occupying the pore space are, at least in the short-term, restricted from moving in or out of the formation in response to these stress changes. The fluids instead carry parts of the stress change and consequenctly experience changes in pore pressure. The aim of the current study is to investigate means of predicting pore pressure generation following changes in surrounding stresses and to compare them to experimental data from a North Sea shale. Using only limited experiemental data and available poroelastic theory, predictions of pore pressure generation under various total stress change scenarios are made. A series of triaxial tests are then performed on the same shale core, and the measured pore pressures are compared to those predicted. The results show that the procedure followed enables accurate prediction of pore pressure development as a function of both material orientation and stress path. These findings highlight how pore pressure changes within anisotropic rocks can be predicted from minimal experimental testing campaigns and provide valuable input to geomechanical modelling of subsurface stress changes.

1 Introduction

Reservoir pore pressure alterations arising from fluid injection or production can cause deformational processes and changes in total stresses within both reservoir and surrounding rocks due to the coupling that exists between pore pressure and stress (e.g. Addis, 1997; Hettema et al., 2000; Teufel et al., 1991; Zoback & Zinke, 2002). These pore pressure- and total stress variations together determine the effective stresses that eventually cause rock deformation (Terzaghi, 1936). Estimation of effective stress evolution for reservoir and surrounding rocks during production or injection is needed to predict mechanical consequences such as reservoir compaction and subsidence/uplift, caprock fracturing, fault reactivation, borehole collapse or casing deformation (e.g. Altmann et al., 2014; Altmann et al., 2010; Angus et al., 2016; Castelletto et al., 2013; Holt et al., 2004; Lynch et al., 2013; Santarelli et al., 1998; Segura et al., 2011; Aadnoy, 1991). Permeable reservoir rocks typically display drained behavior in response to changes in total stresses. However, very little fluid movement occurs in the low-permeable caprocks overlying such reservoirs. Consequently, the caprocks' response to alterations in the stress field will be undrained and can lead to significant pore pressure changes even without fluid movement to or from the reservoir. The amount of undrained pore pressure generation depends on the magnitude and direction of the total stress change and the material's poroelastic parameters. Poroelastic theory addresses the coupling between fluid flow and mechanical deformation of fluid-saturated rocks (e.g. Biot, 1941; Cheng, 2016; Wang, 2017). Within the poroelastic framework, Skempton's pore pressure parameters, As and Bs, predict the undrained pore pressure generation in response to deviatoric and isotropic stress changes, respectively (Skempton, 1954). Understanding these pore pressure parameters and what affects them is thus crucial to explain effective stress changes in caprocks. In anisotropic poroelastic theory, the

directional dependency of properties found in most sedimentary rocks are included (e.g. Biot, 1955; Carroll, 1979; Cheng, 2016; Holt, Bakk, & Bauer, 2018; Thompson & Willis, 1991). As a result, Skempton's pore pressure parameter Bs is generalized into a second rank tensor, where the effect of pore pressure by deviatoric stresses is similar to that of As.

One consequence of Skempton's original formulation is that the amount of undrained pore pressure generated depends on the ratio between changes in minor ($\Delta\sigma 3$) and major ($\Delta\sigma 1$) principal stresses (i.e. the stress path). In fact, a linear relationship is predicted between the pore pressure change normalized to the total vertical stress change and the stress path (Skempton, 1954). For anisotropic rocks, the influence of relative orientation between principal stresses and material symmetry axis on pore pressure generation from deviatoric stress changes can be predicted from the components of the tensorial Bij (Cheng, 2016; Holt, Bauer, et al., 2018). Both the relationship between stress path and normalized pore pressure and the directional dependence of Skempton's As have previously, to a limited extent, been experimentally evaluated for shales (Holt, Bakk, Stenebråten, et al., 2018; Holt, Bauer, et al., 2018). However, to our knowledge, the literature is missing studies combining these two dependencies and thereby enabling a more comprehensive pore pressure forecasting on a well characterized shale. In the current study, the aim is to demonstrate experimentally that the effects of both stress path and stress orientation on pore pressure generation in a low-permeable, anisotropic rock can be predicted using poroelastic theory and require only minimal data form laboratory testing. The experimental work is performed in the triaxial apparatus with shale samples from the North Sea Draupne Formation. Parameters needed to construct the pore pressure predictions are first derived from a single test on a sample with known orientation. Then, a series of undrained tests following different total

stress paths are performed on samples subcored with different sample axis orientations relative to the originally horizontal rock layering. The target is to investigate how measured undrained pore pressure alterations match those predicted by poroelastic theory for various stress paths and stress orientations. If reliable predictions can be made, it demonstrates that relatively simple experimental procedures can be used to obtain data needed to model pore pressure changes under a variety of different field conditions.

2 Poroelastic theory and undrained pore pressure generation

The mechanical properties of rocks are affected by the presence of fluids that can move within their porous frames, and poroelastic theory can describe the constitutive behavior of fluid-saturated rocks. Whether or not fluids can leave or enter the pores of rocks subjected to stress changes determine if the material behaves drained or undrained, respectively. If drainage is permitted, the fluid will not take part in the load-bearing process, and any deformation occurring will be the result of deformation of the solid constituents and the porous structure. If drainage is prohibited, fluids occupying the pore space provide additional resistance to stress changes. In such cases, stress variations will be partly transferred to the fluid pressure which will change in response. Skempton (1954) introduced the pore pressure parameters A_s and B_s to quantify the undrained pore pressure change (Δu) of saturated soils during undrained loading. The formulation in Equation 1 was made for stress conditions known as compressional triaxial conditions in which $\Delta\sigma_1$ and $\Delta\sigma_3$ define changes in major and minor principal stresses, respectively (and $\Delta\sigma_2 = \Delta\sigma_3$):

$$\Delta u = B_s[\Delta\sigma_3 + A_s(\Delta\sigma_1 - \Delta\sigma_3)] \qquad \text{Equation 1}$$

Skempton's B_s-parameter represents the ratio of undrained pore pressure to change in mean stress ($\left(\frac{2\Delta\sigma_3+\Delta\sigma_1}{3}\right)$) and varies with the rock frame compressibility (C) relative to that of the pore fluid (C_f) and solid constituents (C_s). In Equation 2, Skempton's B_s-parameter is expressed as a function of these compressibilities and the porosity (n) (Kümpel, 1991):

$$B_s = \frac{1}{1 + n\left(\frac{C_f - C_s}{C - C_s}\right)} \qquad \text{Equation 2}$$

Skempton experimentally showed that the parameter B_s is close to unity for saturated and unconsolidated sediments where the frame compressibility significantly exceeds that of the fluids. Materials containing more compressible pore fluids (e.g. gas) or a relatively increased frame stiffness compared to the solids (e.g. rocks) will have B_s-values less than 1.

Skempton's A_s describes the undrained pore pressure response to deviatoric stress changes (i.e. the difference between $\Delta\sigma_1$ and $\Delta\sigma_3$). If a rock is assumed to be isotropic and to follow linear poroelasticity, the pore pressure response is entirely controlled by mean stress ($\Delta u = 1/3(\Delta\sigma_1 + 2\Delta\sigma_3)$) and Skempton's A_s equal to 1/3. However, from Skempton's original experiments on various types of clays, a range of A_s-values from -0.5 to 1.5 was measured. The variation in A_s was attributed to the non-elastic nature of clays.

In the case of compressional triaxial stress conditions, it is convenient to replace the major and minor principal stresses with vertical and horizontal stresses, respectively. In the

current study, discussions are limited to cases where the minor and intermediate principal stresses (horizontal stresses) are equal and smaller than the vertical stress (i.e. $\Delta\sigma_v > \Delta\sigma_H = \Delta\sigma_h$). Furthermore, the ratio of changes in minor and major principal stresses is described by the stress path parameter κ:

$$\kappa = \frac{\Delta\sigma_h}{\Delta\sigma_v} \qquad \text{Equation 3}$$

By rearranging Skempton's formulation given in Equation 1 and including the stress path parameter κ, it is shown that the undrained pore pressure normalized to the vertical stress increment is linearly connected to κ:

$$\frac{\Delta u}{\Delta\sigma_v} = \big(B_s(1 - A_s)\big)\kappa + A_s B_s \qquad \text{Equation 4}$$

Equation 4 signify that different undrained stress paths generate varying pore pressure. A consequence of Equation 4 is therefore that if the pore pressure parameters A_s and B_s are known, the undrained pore pressure arising from stress changes along any compressional stress path can be predicted.

So far, the discussion has been limited to isotropic rocks. However, most rocks have a directional dependency in their properties. For anisotropic materials, it is known that undrained

pore pressure generation varies with stress orientation relative to any symmetry direction that exists in the rock (Cheng, 2016). Horizontally layered rocks, such as shales (Piane et al., 2011), are often treated as vertical transverse isotropic (VTI) materials with equal properties in the horizontal plane and different properties in the vertical direction (Fjær et al., 2008). By utilizing anisotropic poroelastic stress-strain relations (and the inverse strain-stress relations) in a similar manner as for anisotropic elasticity, Biot's fluid strain parameter (ζ) can be expressed by the stress tensor (σ_{ij}), pore pressure (u) and Hooke's law constants (C and B_{ij}) (Cheng, 1997):

$$\zeta = C(u + \frac{1}{3}B_{ij}\sigma_{ij}) \qquad \text{Equation 5}$$

The fluid strain parameter gives the fluid volume leaving or entering the solid frame per unit volume of solid frame. In the case of undrained stress change with no shear-induced volume change of the solid frame, ζ is zero and Equation 5 reduces to the first part of Equation 1 in which B_{ij} can be viewed as a generalization of Skempton's B_s into a second rank tensor (Cheng, 1997; Cheng, 2016; Holt, Bakk, Stenebråten, et al., 2018; Thompson & Willis, 1991). For vertical transverse materials, the tensorial B_{ij} consists of two independent components, B_v and B_h. Subscripts v and h refer to vertical and horizontal, or perpendicular and parallel to the symmetry plane in VTI materials, respectively (Cheng, 1997):

$$\Delta u = \frac{1}{3}B_{ij}\Delta\sigma_{ij} = \left(\frac{2B_h + B_v}{3}\right)\left(\frac{2\Delta\sigma_h + \Delta\sigma_v}{3}\right) \qquad \text{Equation 6}$$

184 According to Cheng (1997), the significance of Equation 6 is that pore pressure can be
185 generated by incremental normal as well as shear stress, the latter being an effect similar to the
186 concept of Skempton's A_s parameter. The undrained pore pressure response to an isotropic stress
187 change ($\Delta\sigma_{iso} = \Delta\sigma_h = \Delta\sigma_v$) is independent of material orientation relative to the symmetry
188 axis, since $B_{ij} = B_s$ is expressed as a volume-weighted average of the two invariant components
189 (Holt et al., 2017). However, the undrained pore pressure generated from an anisotropic stress
190 change depends on stress orientation. If θ denotes the angle between symmetry axis and major
191 principle stress direction, the undrained pore pressure response in a triaxial compression test can
192 be predicted by Equation 7 (Holt, Bakk, Stenebråten, et al., 2018):

193

$$\Delta u = B_s \left[\Delta\sigma_3 + \frac{(B_h sin^2\theta + B_v cos^2\theta)}{2B_h + B_v} (\Delta\sigma_1 - \Delta\sigma_3) \right] \qquad \text{Equation 7}$$

194 Equation 7 resembles the formulation by Skempton in Equation 1, with A_s displaying a
195 directional dependence given by the B_s tensorial components:

196

$$A[\theta] = \frac{(B_h sin^2\theta + B_v cos^2\theta)}{2B_h + B_v} = \frac{(B_h sin^2\theta + B_v cos^2\theta)}{3B_s} \qquad \text{Equation 8}$$

197 Worth noting is that the subscript *s* is herein reserved for the original Skempton's A_s
198 parameter. Since the tensorial B_{ij} equals B_s for VTI materials under triaxial stress conditions, the
199 two are used interchangeably. However, *A[θ]* is an elastic parameter, in contrast to Skempton's
200 original A_s (Raaen et al., 2019). Combining Equation 4 and Equation 8 thus allows for theoretical

predictions of normalized pore pressure to be made from the tensorial components of Skempton's B_s on VTI materials oriented at all directions relative to rock layering and exposed to elastic loading along all different compressive stress paths:

$$\frac{\Delta u}{\Delta \sigma_v} = \left(\frac{2B_h + B_v}{3}\right) * (1 - A[\theta]) * \kappa + A[\theta] * \left(\frac{2B_h + B_v}{3}\right) \qquad \text{Equation 9}$$

B_s-value measurements on saturated shales found in the literature typically vary between 0.5 and 0.9 (e.g. Belmokhtar et al., 2016; Mohajerani et al., 2011;Favero et al., 2018; Giger et al., 2018; Lozovyi & Bauer, 2019; Wild et al., 2017;Holt, Bauer, et al., 2018; Ma & Gutierrez, 2020). Soldal et al. (2021b) previously reported B_s-values between 0.52 and 0.71 for the Draupne shale. There are fewer reports of Skempton's A_s from laboratory testing on low-permeable rocks in the literature. One example is from Lozovyi and Bauer (2019) who measured A_s-values between 0.13 and 0.6 during triaxial testing on sandy and shaly facies of Opalinus Clay. Their testing on samples subcored with different angles between sample axis and rock layering also clearly showed that the undrained pore pressure during deviatoric loading varied with the sample orientation. Even less experimental data has been reported from studies seeking to demonstrate the directional variations in *A[θ]* predicted by anisotropic poroelastic theory. Cheng (1997) used the laboratory data collected by Aoki et al. (1993) to compute tensorial B_s-value components of the Trafalgar shale from triaxial testing (B_h = 0.51 and B_v = 0.63). The components were not, however, used to predict undrained pore pressure variation with orientation. Holt, Bakk, Stenebråten, et al. (2018) reported anisotropic poroelastic coefficients from several different, unspecified shales. For a field core of 'soft shale', the horizontal and vertical B_s-value

components were experimentally determined to 0.57 and 1.33, respectively. $A[\theta]$-values measured in undrained triaxial experiments on samples with different orientations were in line with those predicted from the B_s-value components. A similar experimental campaign on a more porous overburden field shale showed that Skempton's $A[\theta]$ decreased from 0.6 to 0.2 between samples oriented parallel and perpendicular to the symmetry axis. The novelty of the present study is that the directional variation in $A[\theta]$ is used to predict the pore pressure variation in stress path dependence as a function of orientation.

3 Material

The shale material tested in the current study is from the Draupne Formation, which is considered both one of the main petroleum source rocks and caprocks in the North Sea (Faleide et al., 2010). It belongs to the Viking group and was deposited under anoxic conditions in several over-deepened basins during the Upper Jurassic (Faleide et al., 2010; Færseth et al., 1995; Underhill, 1998; Whipp et al., 2014). Samples tested were extracted from core material collected from well 16/8-3S in the Ling depression. The Ling depression is located south of the Horda platform and separates the basement highs of Utsira and Sele (Fossen & Hurich, 2005; Færseth et al., 1995). From the well, 9 meters of Draupne core material was retrieved from a depth of 2574.5 – 2583.5 m MD. The mineralogy and mechanical properties of the Draupne core material from this well have been characterized by several authors in recent studies (e.g. Bohloli et al., 2020; Koochak Zadeh et al., 2017; Skurtveit et al., 2015; Smith, 2019; Soldal et al., 2021a). The clay content of the Draupne shale is approximately 50 % and the total organic content is between 6 and 8 wt.%. Due to the low hydraulic permeability (10^{-15} m/s) and high CO_2 capillary breakthrough pressure (≈ 4 MPa) (Skurtveit et al., 2012), intact Draupne shale is expected to make an excellent caprock above potential CO_2 storage formations in the North Sea. The

245 porosity ranges between 13 – 17 % and the average bulk density is 2.25 g/cm^3. Assumed vertical
246 and horizontal effective in-situ stresses for the core material used in the current study is 26.1 and
247 17.2 MPa, respectively (Koochak Zadeh et al., 2017), and the material is considered normally to
248 slightly overconsolidated (Soldal et al., 2021a).

249 **4 Method**

250 4.1. Sample preparation

251 Since shales are highly sensitive to changes in saturation (e.g. Ewy, 2015, 2018; Valès et
252 al., 2004), the Draupne core material has been kept submerged in mineral oil since retrieval to
253 prevent drying. Recent fluid content measurements after several years of storage showed no
254 change in saturation (Soldal et al., 2021a). Core sections from which triaxial rock samples were
255 prepared were initially separated from the remaining core using a circular saw. The end surfaces
256 of the core sections were then made parallel and planar using a grinding machine in a controlled
257 humidity environment. Next, cylindrical samples were sub-cored using an oil-cooled, custom-
258 made drill bit with an internal, air-pressure supported piston maintaining a small, constant axial
259 load on the sample during drilling. Immediately after completion of the coring procedure, the
260 samples were inspected for visible fractures, before they were placed inside a small aluminum
261 rack providing some vertical support and submerged in oil until testing. The tested samples had
262 diameters of 25 mm and height to diameter ratio from 2 - 2.5:1. Prior to testing, the samples'
263 surfaces were wiped free of mineral oil using oil-only absorbent pads.

264

4.2. Experimental device

Testing was done inside a traditional type of triaxial pressure cell where changes in confining pressure normally cause equal changes in vertical and horizontal stresses. Deviatoric stresses is supplied by a stepping motor located beneath the cell base, and confining pressure and top and bottom pore pressures are independently controlled by hydraulic pressure controllers. Vertical and horizontal sample deformations are measured internally inside the cell over the middle third of the sample height using two vertical and two horizontal Linear Variable Differential Transducers (LVDTs). Vertical load is measured internally by a vented load sensor located just beneath the bottom end piece. The membrane surrounding the sample is made of a material that prevents water diffusion from the rock sample without being too stiff. Four vertical side drains connecting the porous filters at the top and bottom were used for radial drainage to speed up pore pressure equilibration. A more detailed description of the equipment used can be found in Berre (2011) and Soldal et al. (2021a). During undrained testing, the measured pore pressure will be affected by the presence of a non-zero dead-volume with a certain compressibility between the sample and the closed valve(s) (e.g. Bishop, 1976; Ghabezloo & Sulem, 2008; Ghabezloo & Sulem, 2010; Wissa, 1969). Efforts have been made to reduce the dead-volume by using only 1/16" steel tubing and by keeping the length of the tubing at a minimum. The 70 MPa pore pressure sensor, having an accuracy of 0.05 % of full scale, between the sample and the drainage valve has also been modified to contain a minimal internal fluid volume. The compressibility of the drainage system was evaluated by measuring the volume needed to pressurize the system with only a steel dummy inserted into the triaxial cell, both with open and closed drainage valves. The difference between the two can be used together with the absolute volume of the drainage system to calculate compressibility. The procedure described by

Ghabezloo and Sulem (2008) for system compliance evaluation indicate that compliance of the current testing system would result in a corrected Skempton's B_s-value less than 10 % higher than the measured. Due to the relatively small error introduced by the none-zero dead volume and the differences in testing procedures followed in the current study, however, the corrections are not applied to the results presented herein.

4.3. Test procedures

Results from a total of nine triaxial tests are presented in the current study (see Table 1). The purpose of Test 1 was to derive the parameters needed to predict pore pressure variation as a function of stress path and orientation, whereas the purpose of all the other tests was generate experimental data to compare to the predictions. Test 1 was done on a sample with its axis parallel with the symmetry axis, and the experimental procedure followed will be described in detail later. To investigate potential effects of consolidation conditions on the generated pore pressure, the anisotropic consolidation in Test 1 was replaced by isotropic consolidation in Test 2. In Tests 3 and 4, the same procedure as in Test 1 was followed for samples with orientation $\theta = 90°$. The reason for doing two identical tests here was to evaluate potential influence of heterogeneity between samples. Results from Tests 5 – 9 have previously been reported by Skurtveit et al. (2015) and Soldal et al. (2021b) and will only be briefly described here. It is emphasized that only Test 1 was needed to formulate the pore pressure predictions; the purpose of the remaining tests was to evaluate experimentally the applicability of those predictions.

310

			Consolidation		Elastic stress cycles			
Test #	**θ (°)***	**φ (%)****	**Iso.**	**Aniso.**	**1st cycle κ**	**2nd cycle κ**	**3rd cycle κ**	**4th cycle κ**
Test 1	0	14.2		✓	1	0.7	0	-0.5
Test 2	0	13.4	✓		1	0.5	0	-0.5
Test 3	90	15.9		✓	1	0.7	0	-0.5
Test 4	90	16.1		✓	1	0.7	0	-0.5
Test 5	0	13.9	✓		×			
Test 6	30	16.4	✓		×			
Test 7	45	15.8	✓		×			
Test 8	60	16.2	✓		×			
Test 9	90	16.3	✓		×			

311 Table 1: Overview of the 9 triaxial tests included in the current study. * Orientation given as the
312 angle θ between the major principal stress direction and the symmetry axis. ** Initial porosity
313 calculated from the initial and final fluid contents and a grain density of 2.55 g/cm^3.
314

315 The experimental protocol followed in Test 1 is schematically illustrated in Figure 1. The
316 confining pressure was immediately increased to 1 MPa after inserting the sample surrounded by
317 four side drains and the sleeve into the triaxial cell. The vertical stress was then increased to give
318 the correct in-situ ratio between principal stresses. Next, the stresses were simultaneously
319 increased to the absolute values of the in-situ effective stresses (σ_v' = 26.1 MPa and σ_h' = 17.2
320 MPa). Degassed analog pore fluid (NaCl = 37 g/l) could now enter the porous end filters and
321 flushed through the side drains. Then the backpressure was increased to the in-situ pore pressure
322 of 27.9 MPa (rate 0.6 MPa/hr), whilst maintaining constant horizontal and vertical effective
323 stresses. After this, a minimum of 40 hours was given for the sample pore pressure to equilibrate
324 before the tests proceeded.

The valve between the backpressure system and the sample was then closed in Test 1, leaving the samples under undrained conditions. The sample was subsequently subjected to four stress cycles, each following a different stress path; isotropic, uniaxial strain, uniaxial stress and constant mean stress path. In all stress cycles, the total vertical stress increment was 4 MPa and was applied over a period of 8 hours. After completion of the total vertical stress increase, a minimum of 10 hours was granted for equilibration of excess pore pressure before the stress was decreased again at the same rate ($\Delta\dot{\sigma}_v$= 0.5 MPa/hour). In the isotropic stress cycle, the total horizontal stress increment was equal to the total vertical stress increment, in the uniaxial strain cycle the total horizontal stress was adjusted to prevent horizontal sample deformation, in the uniaxial stress cycle there was no change in total horizontal stress, whereas in the constant mean stress cycle the total horizontal stress increment was – 0.5 times the total vertical stress increment (maintaining $\frac{2\Delta\sigma_h+\Delta\sigma_v}{3} = 0$). Between all stress cycles, drainage was re-opened, and the pore pressure controlled at the initial value of 27.9 MPa. The pore pressure was controlled for a minimum of 8 hours before the drainage valve was again closed and the next stress cycle initiated.

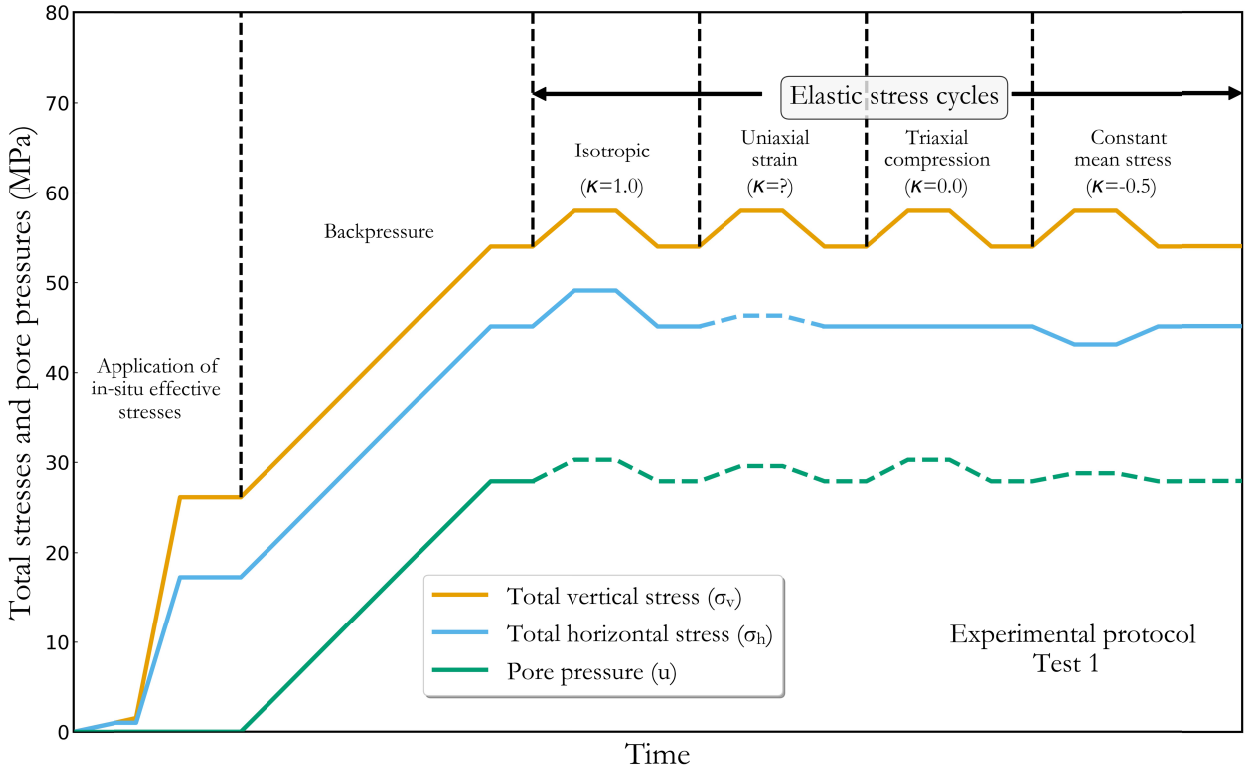

Figure 1: Schematic illustration of the triaxial testing procedure followed in Test 1 (θ=0°). The effective in-situ stresses were σ_v' = 26.1 MPa and σ_h'= 17.2 MPa and the backpressure was 27.9 MPa. The total vertical stress increments in all four elastic load cycles were 4 MPa. The same procedure was also followed in Test 2, with the exception that consolidation was isotropic (σ' = 23.5 MPa) and the backpressure was 20 MPa. In Tests 3 and 4, the procedure in Figure 1 was reproduced on samples with (θ = 90°).

In Test 2, the effective isotropic consolidation stress and backpressure was 23.5 and 20 MPa, respectively. Instead of a uniaxial strain load cycle, the second load cycle in Tests 2 – 4 was replaced with a constant stress path parameter cycle (κ = 0.5 and 0.7 for Tests 2 and 3 & 4, respectively). In Tests 5 – 9 samples of different orientations were isotropically consolidated and subjected to undrained shearing. The effective consolidation stresses and backpressures in Tests 5 – 9 were 20 and 30 MPa, respectively. Undrained shearing was done by increasing the vertical stress to give a specified axial strain rate. A very low axial strain rate (10^{-9} s^{-1}) was used to ensure that the generated undrained pore pressure had ample time to equilibrate within the

sample pore volume (Soldal et al., 2021b). The only measurements from Tests 5 – 9 used in the current study, are the pore pressure changes relative to the increase in total vertical stresses between the start of shearing and sample failure.

5 Results

The undrained pore pressures (Δu) generated in each of the four stress cycles in Tests 1 – 4 are plotted against the change in total vertical stress ($\Delta\sigma_v$) in Figure 2. Figure 2a and b show the results from Tests 1 and 2 with sample axis perpendicular to layering, whereas Figure 2c and d are from tests 3 and 4 with samples oriented parallel with layering. In the same plots, the ratios of maximum pore pressure change to total vertical stress change are given as single values (i.e. 'normalized pore pressure' = $\Delta u/\Delta\sigma_v$). It is observed that the changes in undrained pore pressure during the isotropic stress cycles in all tests have similar magnitude, demonstrating that Skempton's B_s is independent of material orientation. Furthermore, results show that gradually less pore pressure is generated going from the isotropic to the constant mean stress cycle (i.e. reducing κ). In Tests 1 and 2, the pore pressure generation relative to the total vertical stress increment when the mean stress is kept constant is less than half of that during the isotropic stress cycle. Results show very little difference in terms of pore pressure generation between the anisotropically (Test 1) and isotropically (Test 2) consolidated tests on samples with identical orientation. During the uniaxial strain cycle in Test 1, the change in total horizontal stress needed to prevent changes in horizontal deformation resulted in a secant stress path parameter κ of 0.7. This stress path was used when controlling the second stress cycles in Tests 3 and 4. The reduction in generated pore pressure from isotropic to constant mean stress cycle is larger in Tests 3 and 4 compared to Tests 1 and 2. During loading (i.e. increasing total vertical stress)

under constant mean stress conditions, the pore pressure in fact decreased. Also, worth noting is that pore pressure after unloading generally returned back to values close to the pore pressure before loading was initiated.

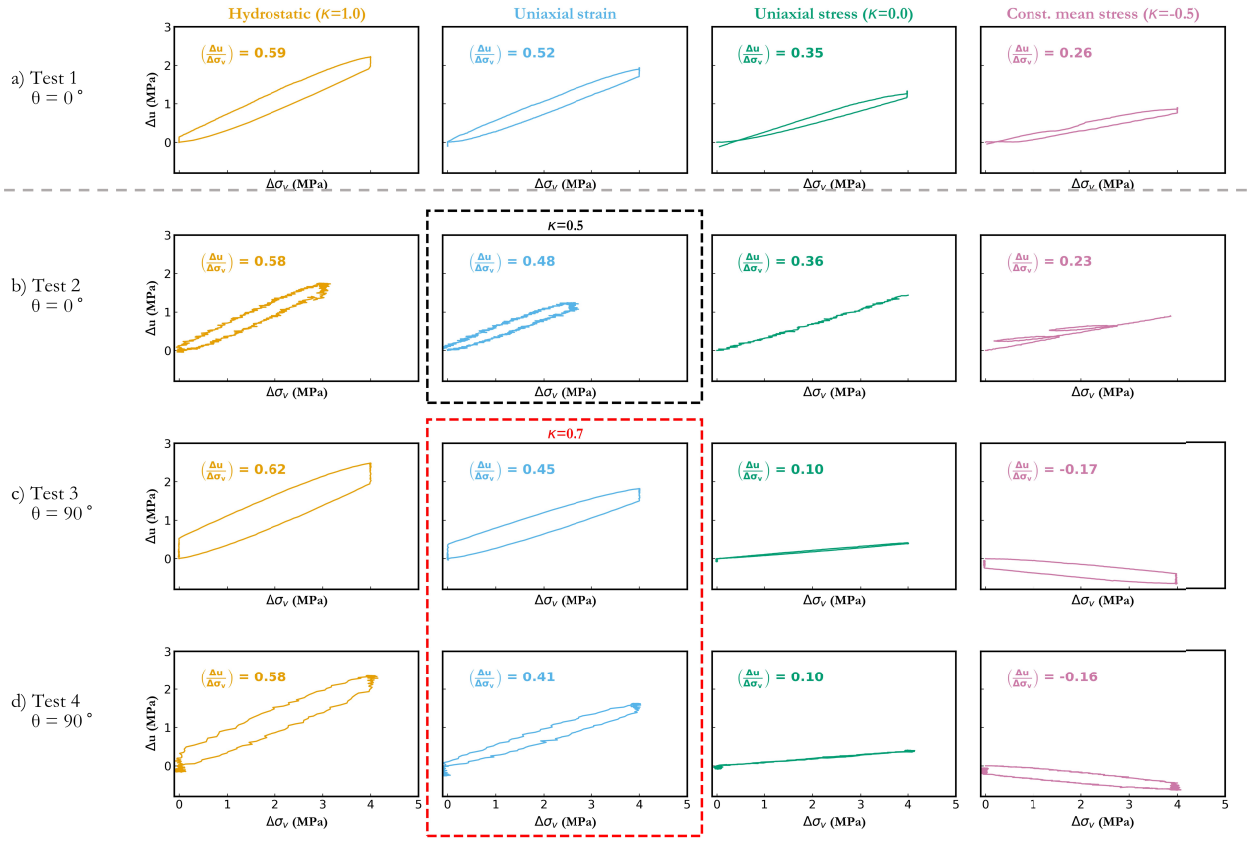

Figure 2: a) Pore pressure generation versus change in total vertical stress measured in Test 1 (θ = 0°) during undrained hydrostatic, uniaxial strain, uniaxial stress and constant mean stress cycles. b) Pore pressure generation versus change in total vertical stress measured in Test 2 (θ = 0°) during undrained hydrostatic, κ = 0.5, uniaxial stress and constant mean stress cycles. c) Pore pressure generation versus change in total vertical stress measured in Test 3 (θ = 90°) during undrained hydrostatic, κ = 0.7, uniaxial stress and constant mean stress cycles. d) Pore pressure generation versus change in total vertical stress measured in Test 4 (θ = 90°) during undrained hydrostatic, κ = 0.7, uniaxial stress and constant mean stress cycles.

One of the aims of the current study is to examine whether reliable predictions of undrained pore pressure variation with orientation can be made using components of the tensorial B_s parameter. To this end, the horizontal and vertical components need first to be

quantified. Figure 3 plots the undrained pore pressure normalized to the change in total vertical stress against stress path parameter κ for Tests 1 and 2. Results from both tests display the same linearity predicted by Skempton's formulation, and any possible influence of isotropic as opposed to anisotropic consolidation on pore pressure generation is therefore considered negligible. The resulting slope and intercept from linear regression can be used together with Equation 4 to calculate Skempton's A_s and B_s values of 0.61 and 0.59, respectively. Since the sample orientation is known (θ = 0°), Skempton's B_s can then be divided into a horizontal component of 0.34 and a vertical component of 1.09 using Equation 6 and Equation 8.

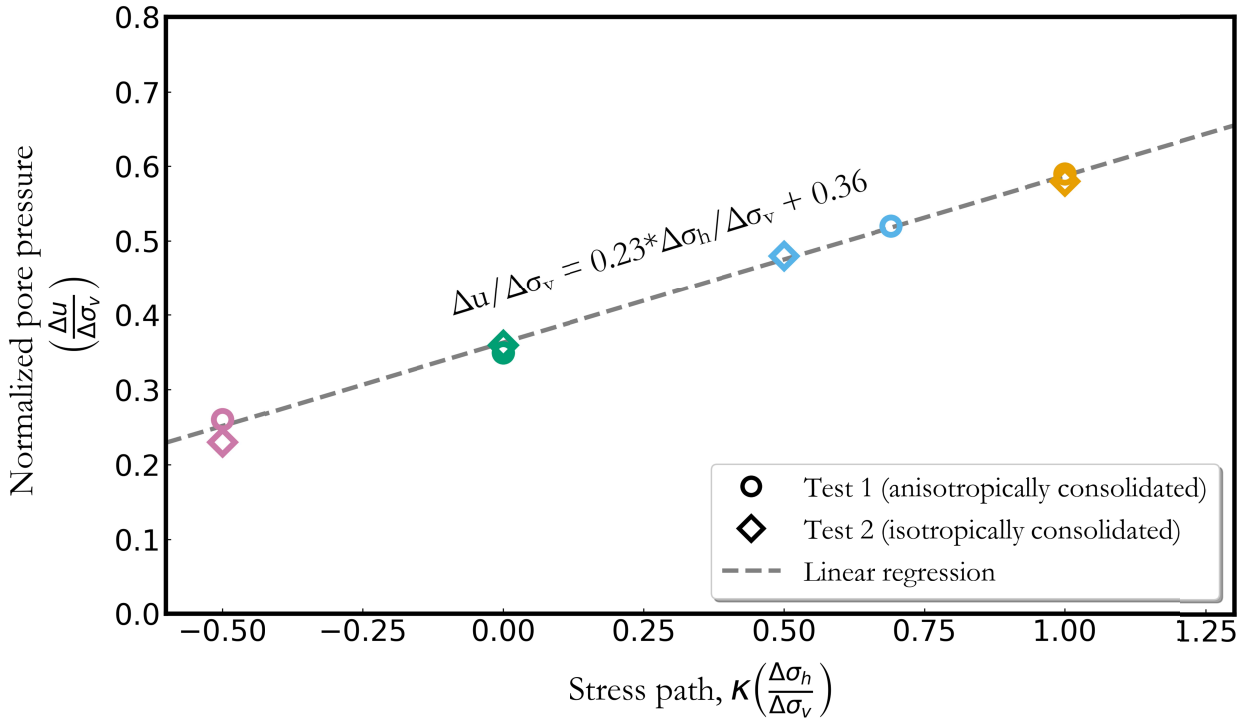

Figure 3: Normalized pore pressure plotted against the stress path parameter κ for Tests 1 and 2 (θ = 0°). Open circles are drawn from the anisotropically consolidated Test 1 and open diamonds are drawn from the isotropically consolidated Test 2. The result of linear regression given above the dashed line.

410 The generated pore pressures during undrained shearing of samples with different
411 orientation in Tests 5 – 9 are plotted against changes in total vertical stress in Figure 4a. As the
412 angle between the sample axis and the symmetry axis increases, the generated pore pressure
413 decreases. The total undrained pore pressure in Test 5 ($\theta = 0°$) is almost 2.5 times that in Test 9
414 ($\theta = 90°$). To calculate A_s from Tests 5 – 9, the secant total pore pressure change recorded
415 between the initiation of shearing and sample failure (defined as the highest measured shear
416 stress) was first divided by the corresponding change in total vertical stress. The result is equal to
417 the product of Skempton's two pore pressure parameters, and A_s was then found by dividing this
418 by $B_s = 0.59$. The calculated A_s values are plotted as open circles in Figure 4b. The predicted
419 variation in $A[\theta]$ based on B_s-value components and Equation 8 is represented by the dashed line
420 in the same figure. Figure 4b shows that the poroelastic expression of $A[\theta]$ made up of the B_s-
421 value components can be used to accurately predict undrained pore pressure generation as a
422 function of material orientation, even in cases where significant plastic deformation most
423 probably has occurred (i.e. $A_s \approx A[\theta]$).
424
425

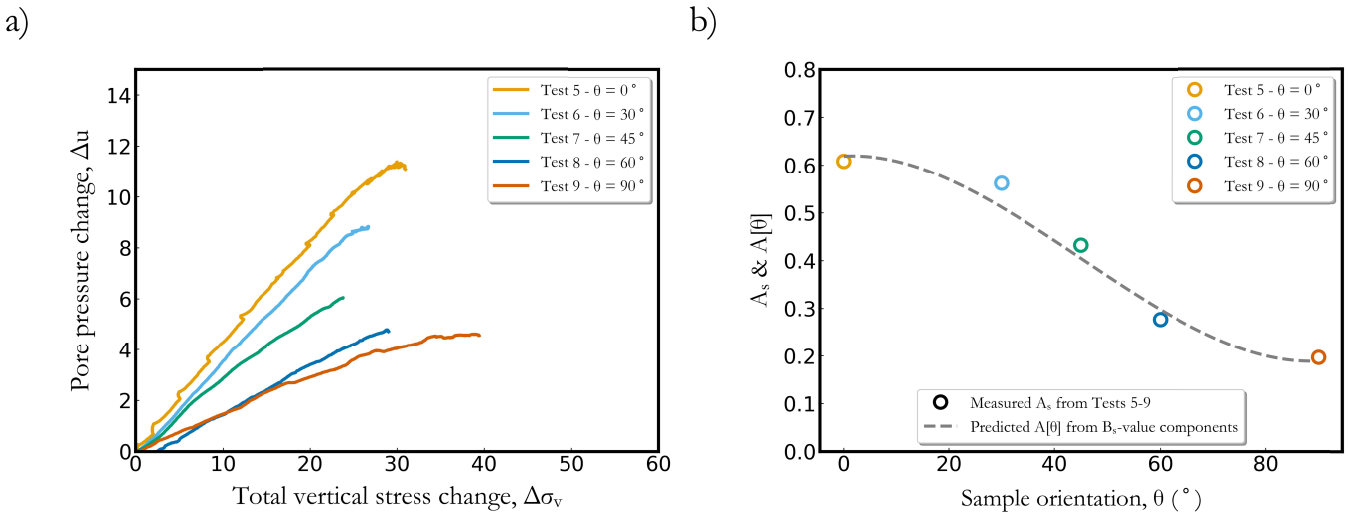

Figure 4: a) Measured pore pressure change plotted against change in total vertical stress during undrained shearing of the isotropically consolidated samples in Tests 5 – 9. The orientation of sample axis relative to symmetry axis for each test is given in the figure legend. b) Values of A_s from Tests 5 – 9 plotted as open circles together with the predicted variation in A [θ] based on B_s-value components.

Once it is demonstrated that the variation in Skempton's A_s with material orientation can be predicted from the tensorial B_s components, the next step is to examine how the relationship between normalized pore pressure and stress path will vary with orientation. The dashed lines in Figure 5 are predictions of how the normalized pore pressures will vary as functions of stress path based on a constant B_s-value and A_s-values changing with orientation. The orange line is drawn for samples oriented with θ = 0° and the blue line for samples oriented with θ = 90°. The diamond markers representing measured values in Tests 1 – 4 follow the predicted trends extremely well. Furthermore, the consistency between Tests 1 & 2 and 3 & 4 indicates both the applicability of the current method and that there is no significant heterogeneity between the tested samples.

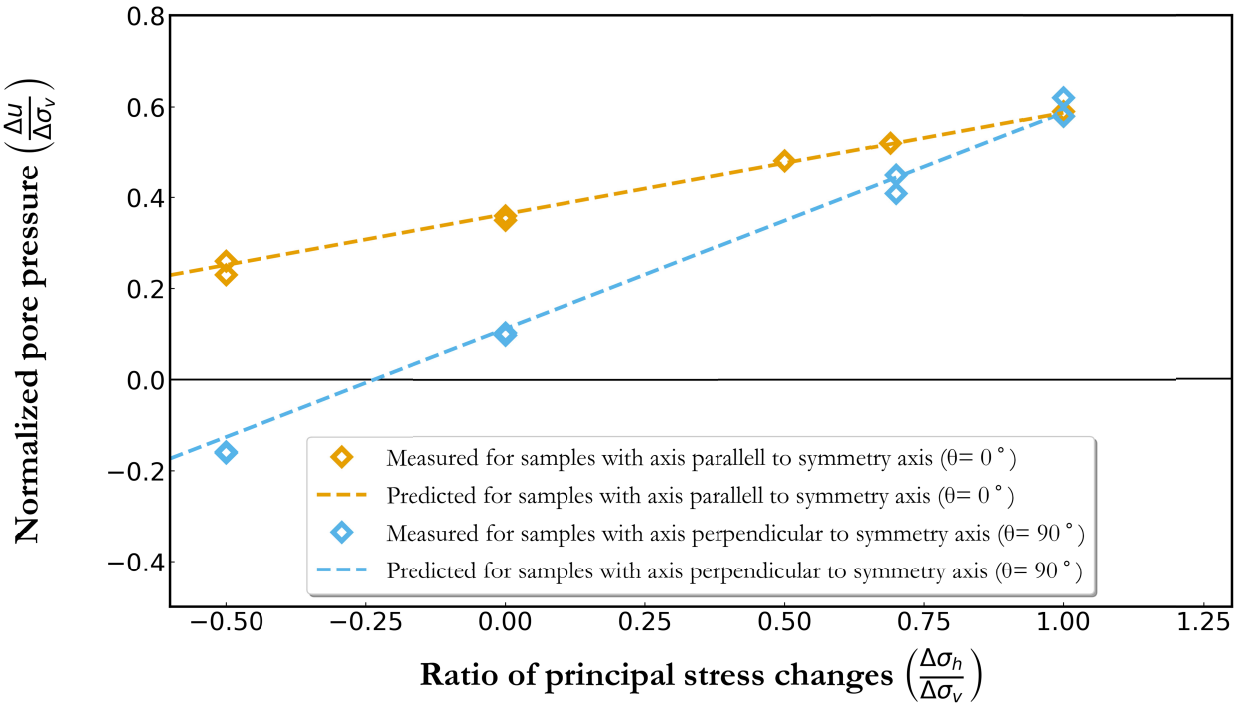

443

444 Figure 5: Predicted normalized pore pressure as a function of stress path in dashed lines. Orange
445 line predicts the linear relationship for samples with sample axis parallel to the symmetry axis,
446 and blue line for samples with axis perpendicular to symmetry axis. Orange and blue diamonds
447 show the measured normalized undrained pore pressures in Tests 1 – 4.

448 **6 Discussion**

449 The objective of the current study was to examine experimentally predictions of
450 undrained pore pressure in a typical North Sea shale exposed to varying stress paths and stress
451 orientations. Using components of the tensorial B_s parameter, the effect of stress orientation on
452 pore pressure generation from deviatoric stress changes were predicted. Subsequent
453 measurements of pore pressure in undrained triaxial tests on samples subcored at different angles
454 relative to the layering in the rock were in accordance with the predictions. Then a linear
455 relationship between undrained normalized pore pressure and stress path was demonstrated on a
456 sample with its axis parallel to the material symmetry axis. Knowing how Skempton's A_s varied
457 with orientation, the effect of stress direction on the relation between normalized undrained pore

458 pressure and stress path was predicted. Again, the predicted pore pressure generation was
459 reproduced in undrained tests on samples with their axis oriented perpendicular to the symmetry
460 axis. The importance of what is presented in Figure 5 is that from relatively simple undrained
461 stress cycling of one sample with a known orientation, the pore pressure generation for all
462 orientations and compressional stress paths of that same material can be accurately predicted
463 using Equation 9.

464

465 The results shown herein demonstrate that significant variation in induced pore pressure
466 generation as a function of stress orientation and stress path can be expected and should be
467 accounted for. The importance of including anisotropy in poroelastic parameters when predicting
468 undrained pore pressure generation has been examined in recent studies by Raaen et al. (2019).
469 They investigated numerically differences in predicted undrained pore pressure around a
470 horizontal borehole in an anisotropic material using isotropic versus anisotropic Skempton's B_s.
471 In the isotropic case, the components of B_s are equal, whereas for the anisotropic case the B_s-
472 value components were estimated from a given set of elastic material properties. Simulations
473 showed that whether choosing isotropic scalar B_s or anisotropic tensorial B_s would significantly
474 affect pore pressure predictions. Since the formation considered was assigned anisotropic elastic
475 properties, it must be assumed that the anisotropic solution was closer to reality than the isotropic
476 simplification.

477

478 Asaka and Holt (2021) compared an anisotropic approach with a conventional approach
479 in terms of predicting unwanted borehole instability during drilling operations. The conventional
480 method assumes isotropic rock properties and ignores pore pressure changes resulting from total

481 stress changes. Both anisotropy in elastic properties and pore pressure parameters were respected
482 in the anisotropic approach. Considerable differences in predicted failure regions and modes
483 resulted from the comparison of the two approaches. Field observations of wellbore failure in
484 shale section at the sides of highly inclined boreholes were only forecasted if anisotropic
485 poroelasticity was included. Furthermore, sensitivity analysis showed that the risk of failure was
486 significantly influenced by the amount of undrained pore pressure, and, accordingly, the
487 anisotropic pore pressure parameters. Skempton parameters used by Asaka and Holt (2021) were
488 estimated from the inverse anisotropic Gassmann's equation. Consequently, there is an
489 uncertainty related to the pore pressure parameters which can only be reduced by more
490 experimental data addressing anisotropic poroelasticity of shales.

491

492 Finally, it is mentioned again that since the influence of plastic deformation on pore
493 pressure parameters is unknown, the predictions herein are strictly speaking limited to loading
494 within the elastic domain. Duda et al. (2021) recently performed experiments to examine how
495 Skempton's pore pressure parameters are affected by plastic deformation. Cyclic triaxial testing
496 of the relatively porous Pierre II shale (φ = 40 %) indicated that although B_s-values remained
497 unaffected throughout shearing, Skempton's A_s reduced quite significantly as the degree of
498 plastic deformation increased. Future research should also consider the potentially variable
499 effects of plastic deformation on pore pressure parameters following different stress paths since
500 this may aid the description of stress evolution in faulted or fractured rock formations.

501

7 Conclusion

This study has shown experimentally that the variation in undrained pore pressure as a function of stress path and stress orientation can be predicted using Skempton's B_s-value components and the stress path parameter κ. A series of undrained triaxial tests on the Draupne Formation shale was designed and executed to enable predictions of pore pressure generation to be made and to later examine experimentally the applicability of those predictions. The tensorial components of B_s were first derived from the measured linear relationship between stress path and normalized pore pressure in one triaxial test on a sample with its axis parallel with the material symmetry axis. Subsequent measurements in five undrained triaxial tests on samples with various relative orientations reproduced the predicted decrease in Skempton's A_s with increasing θ. The variation in A_s with orientation was then incorporated into the relation between normalized undrained pore pressure and stress path. Results from another two tests on samples with their axis perpendicular to the symmetry axis exposed to various stress paths demonstrated that also the variation in stress path dependence as a function of orientation could be forecasted.

The significant variation in pore pressure measured as a function of orientation emphasizes that anisotropic poroelasticity need to be considered to accurately predict undrained pore pressure generation in materials with different properties in different directions. If not, risks related to e.g. borehole stability or caprock fracturing cannot be properly evaluated prior to operations involving fluid injection or production. The experiments herein have shown that tensorial B_s-value components can be very useful in predicting the undrained pore pressure response over a wide range of stress orientation- and stress path scenarios. Even though the predictions do not incorporate any effect of plastic deformation on the pore pressure parameters,

525 the undrained pore pressure in the Draupne shale could be satisfactorily forecasted even in cases
526 involving loading with associated plastic deformations. Characterizing the influence of non-
527 elastic deformation on pore pressure generation is most likely relevant for already fractured or
528 faulted sections of the subsurface and will be subject for future research.
529
530
531
532
533
534
535
536
537
538
539
540
541
542
543
544

References

Addis, M. A. (1997). The Stress-Depletion Response Of Reservoirs. SPE Annual Technical Conference and Exhibition,

Altmann, J. B., Müller, B. I. R., Müller, T. M., Heidbach, O., Tingay, M. R. P., & Weißhardt, A. (2014). Pore pressure stress coupling in 3D and consequences for reservoir stress states and fault reactivation. *Geothermics*, *52*, 195-205. https://doi.org/10.1016/j.geothermics.2014.01.004

Altmann, J. B., Müller, T. M., Müller, B. I. R., Tingay, M. R. P., & Heidbach, O. (2010). Poroelastic contribution to the reservoir stress path. *International Journal of Rock Mechanics and Mining Sciences*, *47*(7), 1104-1113. https://doi.org/https://doi.org/10.1016/j.ijrmms.2010.08.001

Angus, D. A., Fisher, Q. J., Segura, J. M., Verdon, J. P., Kendall, J. M., Dutko, M., & Crook, A. J. L. (2016). Reservoir stress path and induced seismic anisotropy： results from linking coupled fluid-flow/geomechanical simulation with seismic modelling. *Petroleum Science*, *13*(4), 669-684. https://doi.org/10.1007/s12182-016-0126-1

Aoki, T., Tan, C. P., & Bamford, W. E. (1993). Effects of deformation and strength anisotropy on borehole failures in saturated shales. *International Journal of Rock Mechanics and Mining Sciences & Geomechanics Abstracts*, *30*(7), 1031-1034. https://doi.org/10.1016/0148-9062(93)90067-N

Asaka, M., & Holt, R. (2021). Anisotropic Wellbore Stability Analysis: Impact on Failure Prediction. *Rock Mechanics and Rock Engineering*, *54*, 1-23. https://doi.org/10.1007/s00603-020-02283-0

566 Belmokhtar, M., Delage, P., Ghabezloo, S., Tang, A.-M., Menaceur, H., & Conil, N. (2016).
567 Poroelasticity of the Callovo–Oxfordian Claystone. *Rock Mechanics and Rock Engineering*,
568 *50*(4), 871-889. https://doi.org/10.1007/s00603-016-1137-3
569 Berre, T. (2011). Triaxial Testing of Soft Rocks. *Geotechnical Testing Journal*, *34*(1), 61-75.
570 https://doi.org/10.1520/GTJ102879
571 Biot, M. A. (1941). General Theory of Three Dimensional Consolidation. *Journal of applied*
572 *physics*, *12*, 155-164.
573 Biot, M. A. (1955). Theory of Elasticity and Consolidation for a Porous Anisotropic Solid.
574 *Journal of applied physics*, *26*(2), 182-185. https://doi.org/10.1063/1.1721956
575 Bishop, A. W. (1976). The influence of system compressibility on the observed pore-pressure
576 response to an undrained change in stress in saturated rock. *26*(2), 371-375.
577 https://doi.org/10.1680/geot.1976.26.2.371
578 Bohloli, B., Soldal, M., Smith, H., Skurtveit, E., Choi, J. C., & Sauvin, G. (2020). Frictional
579 Properties and Seismogenic Potential of Caprock Shales. *Energies (Basel)*, *13*(6275), 6275.
580 https://doi.org/10.3390/en13236275
581 Carroll, M. M. (1979). An effective stress law for anisotropic elastic deformation. *J. Geophys.*
582 *Res*, *84*(B13), 7510-7512. https://doi.org/10.1029/JB084iB13p07510
583 Castelletto, N., Gambolati, G., & Teatini, P. (2013). Geological CO2 sequestration in multi-
584 compartment reservoirs: Geomechanical challenges. *Journal of Geophysical Research: Solid*
585 *Earth*, *118*(5), 2417-2428. https://doi.org/10.1002/jgrb.50180
586 Cheng, A. H. D. (1997). Material coefficients of anisotropic poroelasticity. *International journal*
587 *of rock mechanics and mining sciences (Oxford, England : 1997)*, *34*(2), 199-205.
588 https://doi.org/10.1016/S0148-9062(96)00055-1

589 Cheng, A. H. D. (2016). *Poroelasticity* (1st ed. 2016. ed., Vol. 27). Springer International
590 Publishing : Imprint: Springer.
591 Duda, M. I., Holt, R. M., Stenebråten, J. F., & Stroisz, A. M. (2021). Effects of Plastic
592 Deformation on Poroelastic Pore Pressure Coefficients in Pierre II Shale. 55th U.S. Rock
593 Mechanics/Geomechanics Symposium,
594 Ewy, R. T. (2015). Shale/claystone response to air and liquid exposure, and implications for
595 handling, sampling and testing. *International Journal of Rock Mechanics and Mining Sciences*,
596 *80*, 388-401. https://doi.org/https://doi.org/10.1016/j.ijrmms.2015.10.009
597 Ewy, R. T. (2018). Practical approaches for addressing shale testing challenges associated with
598 permeability, capillarity and brine interactions. *Geomechanics for energy and the environment*,
599 *14*, 3-15. https://doi.org/10.1016/j.gete.2018.01.001
600 Faleide, J. I., Bjørlykke, K., & Gabrielsen, R. H. (2010). Geology of the Norwegian Continental
601 Shelf. In K. Bjorlykke (Ed.), *Petroleum Geoscience: From Sedimentary Environments to Rock*
602 *Physics* (pp. 467-499). Springer Berlin Heidelberg. https://doi.org/10.1007/978-3-642-02332-
603 3_22
604 Favero, V., Ferrari, A., & Laloui, L. (2018). Anisotropic Behaviour of Opalinus Clay Through
605 Consolidated and Drained Triaxial Testing in Saturated Conditions. *Rock Mechanics and Rock*
606 *Engineering*, *51*(5), 1305-1319. https://doi.org/10.1007/s00603-017-1398-5
607 Fjær, E., Holt, R. M., Horsrud, P., Raaen, A. M., & Risnes, R. (2008). *Petroleum related rock*
608 *mechanics* (2nd ed. ed., Vol. 53). Elsevier.
609 Fossen, H., & Hurich, C. A. (2005). The Hardangerfjord shear zone in SW Norway and the
610 North Sea; a large-scale low-angle shear zone in the Caledonian crust. *Journal of the Geological*
611 *Society*, *162*(4), 675-687. https://doi.org/10.1144/0016-764904-136

612 Færseth, R. B., Gabrielsen, R. H., & Hurich, C. A. (1995). Influence of basement in structuring
613 of the North Sea Basin, offshore southwest Norway. *Norsk geologisk tidsskrift*, *75*, 105-119.
614 Ghabezloo, S., & Sulem, J. (2008). Stress dependent thermal pressurization of a fluid-saturated
615 rock. *Rock Mechanics and Rock Engineering*, *42*(1), 1-24. https://doi.org/10.1007/s00603-008-
616 0165-z
617 Ghabezloo, S., & Sulem, J. (2010). Effect of the volume of the drainage system on the
618 measurement of undrained thermo-poro-elastic parameters. *International journal of rock*
619 *mechanics and mining sciences (Oxford, England : 1997)*, *47*(1), 60-68.
620 https://doi.org/10.1016/j.ijrmms.2009.03.001
621 Giger, S. B., Ewy, R. T., Favero, V., Stankovic, R., & Keller, L. M. (2018). Consolidated-
622 undrained triaxial testing of Opalinus Clay: Results and method validation. *Geomechanics for*
623 *energy and the environment*, *14*, 16-28. https://doi.org/10.1016/j.gete.2018.01.003
624 Hettema, M. H. H., Schutjens, P. M. T. M., Verboom, B. J. M., & Gussinklo, H. J. (2000).
625 Production-Induced Compaction of a Sandstone Reservoir: The Strong Influence of Stress Path.
626 *SPE Reservoir Evaluation & Engineering*, *3*(04), 342-347. https://doi.org/10.2118/65410-PA %J
627 SPE Reservoir Evaluation & Engineering
628 Holt, R., Bauer, A., & Bakk, A. (2017). Overburden pore-pressure changes and their influence
629 on 4D seismic. 2017 SEG International Exposition and Annual Meeting,
630 Holt, R. M., Bakk, A., & Bauer, A. (2018). Anisotropic poroelasticity – Does it apply to shale?
631 https://doi.org/https://doi.org/10.1190/segam2018-2994785.1
632 Holt, R. M., Bakk, A., Stenebråten, J. F., Bauer, A., & Fjær, E. (2018). Skempton's A — A Key
633 to Man-Induced Subsurface Pore Pressure Changes. 52nd U.S. Rock Mechanics/Geomechanics
634 Symposium,

635 Holt, R. M., Bauer, A., & Bakk, A. (2018). Stress Path Dependent Velocities in Shales: Impact
636 on 4D Seismic Interpretation. *Stress Path Dependent Velocities in Shales: Impact on 4D Seismic*
637 *Interpretation*. https://doi.org/https://doi.org/10.1190/geo2017-0652.1
638 Holt, R. M., Flornes, O., Li, L., & Fjaer, E. (2004). Consequences Of Depletion-Induced Stress
639 Changes On Reservoir Compection And Recovery. Gulf Rocks 2004, the 6th North America
640 Rock Mechanics Symposium (NARMS),
641 Koochak Zadeh, M., Mondol, N. H., & Jahren, J. (2017). Velocity anisotropy of upper jurassic
642 organic-rich shales, Norwegian continental shelf.
643 Kümpel, H. J. (1991). Poroelasticity: parameters reviewed. *Geophys. J. Int*, *105*(3), 783-799.
644 https://doi.org/10.1111/j.1365-246X.1991.tb00813.x
645 Lozovyi, S., & Bauer, A. (2019). Static and dynamic stiffness measurements with Opalinus Clay.
646 *Geophysical Prospecting*, *67*(4), 997-1019. https://doi.org/10.1111/1365-2478.12720
647 Lynch, T., Fisher, Q., Angus, D., & Lorinczi, P. (2013). Investigating Stress Path Hysteresis in a
648 CO2 Injection Scenario Using Coupled Geomechanical-fluid Flow Modelling. *Energy Procedia*,
649 *37*, 3833-3841. https://doi.org/https://doi.org/10.1016/j.egypro.2013.06.280
650 Ma, S., & Gutierrez, M. (2020). Determination of the poroelasticity of shale. *Acta geotechnica*,
651 *16*(2), 581-594. https://doi.org/10.1007/s11440-020-01062-z
652 Mohajerani, M., Delage, P., Monfared, M., Tang, A. M., Sulem, J., & Gatmiri, B. (2011).
653 Oedometric compression and swelling behaviour of the Callovo-Oxfordian argillite.
654 *International journal of rock mechanics and mining sciences (Oxford, England : 1997)*, *48*(4),
655 606-615. https://doi.org/10.1016/j.ijrmms.2011.02.016

656 Piane, C. D., Dewhurst, D. N., Siggins, A. F., & Raven, M. D. (2011). Stress-induced anisotropy
657 in brine saturated shale. *Geophysical journal international*, *184*(2), 897-906.
658 https://doi.org/10.1111/j.1365-246X.2010.04885.x
659 Raaen, A. M., Larsen, I., Fjær, E., & Holt, R. M. (2019). Pore Pressure Response in Rock:
660 Implications of Tensorial Skempton B in an Anisotropic Formation. 53rd U.S. Rock
661 Mechanics/Geomechanics Symposium,
662 Santarelli, F. J., Tronvoll, J. T., Svennekjaier, M., Skeie, H., Henriksen, R., & Bratli, R. K.
663 (1998). Reservoir Stress Path: The Depletion and the Rebound. SPE/ISRM Rock Mechanics in
664 Petroleum Engineering,
665 Segura, J. M., Fisher, Q. J., Crook, A. J. L., Dutko, M., Yu, J. G., Skachkov, S., . . . Kendall, J.
666 M. (2011). Reservoir stress path characterization and its implications for fluid flow production
667 simulations. *Petroleum geoscience*, *17*(4), 335-344. https://doi.org/10.1144/1354-079310-034
668 Skempton, A. W. (1954). The Pore-Pressure Coefficients A and B. *4*(4), 143-147.
669 https://doi.org/10.1680/geot.1954.4.4.143
670 Skurtveit, E., Aker, E., Soldal, M., Angeli, M., & Wang, Z. (2012). Experimental investigation
671 of CO2 breakthrough and flow mechanisms in shale. *Petroleum geoscience*, *18*(1), 3-15.
672 https://doi.org/10.1144/1354-079311-016
673 Skurtveit, E., Grande, L., Ogebule, O. Y., Gabrielsen, R. H., Faleide, J. I., Mondol, N. H., . . .
674 Horsrud, P. (2015, 2015/11/13/). *Mechanical testing and sealing capacity of the Upper Jurassic*
675 *Draupne Formation, North Sea* 49th U.S. Rock Mechanics/Geomechanics Symposium, San
676 Francisco, California. https://doi.org/
677 Smith, H. (2019). *Engineering parameters of Draupne shale - Characterization of fractured*
678 *samples and integration with mechanical tests* [Master's thesis, University of Oslo,

679 Soldal, M., Skurtveit, E., & Choi, J. C. (2021a). Laboratory Evaluation of Mechanical Properties
680 of Draupne Shale Relevant for CO2 Seal Integrity. *Geosciences*, *11*(6), 244.
681 https://www.mdpi.com/2076-3263/11/6/244
682 Soldal, M., Skurtveit, E., & Choi, J. C. (2021b). Poroelastic and Mechanical Anisotropy of the
683 Draupne Caprock. 55th U.S. Rock Mechanics/Geomechanics Symposium,
684 Terzaghi, K. v. (1936). The shearing resistance of saturated soils and the angle between the
685 planes of shear. First international conference on soil Mechanics, 1936,
686 Teufel, L. W., Rhett, D. W., & Farrell, H. E. (1991). Effect of Reservoir Depletion And Pore
687 Pressure Drawdown On In Situ Stress And Deformation In the Ekofisk Field, North Sea. The
688 32nd U.S. Symposium on Rock Mechanics (USRMS),
689 Thompson, M., & Willis, J. R. (1991). A Reformation of the Equations of Anisotropic
690 Poroelasticity. *Journal of applied mechanics*, *58*(3), 612-616. https://doi.org/10.1115/1.2897239
691 %J Journal of Applied Mechanics
692 Underhill, J. R. (1998). Jurassic. In *Petroleum Geology of the North Sea* (pp. 245-293).
693 https://doi.org/https://doi.org/10.1002/9781444313413.ch8
694 Valès, F., Nguyen Minh, D., Gharbi, H., & Rejeb, A. (2004). Experimental study of the influence
695 of the degree of saturation on physical and mechanical properties in Tournemire shale (France).
696 *Applied clay science*, *26*(1), 197-207. https://doi.org/10.1016/j.clay.2003.12.032
697 Wang, H. F. (2017). *Theory of Linear Poroelasticity with Applications to Geomechanics and*
698 *Hydrogeology*. Princeton University Press.
699 Whipp, P. S., Jackson, C. A.-L., Gawthorpe, R. L., Dreyer, T., & Quinn, D. (2014). Normal fault
700 array evolution above a reactivated rift fabric; a subsurface example from the northern Horda

Platform, Norwegian North Sea. *26*(4), 523-549.
https://doi.org/https://doi.org/10.1111/bre.12050

Wild, K. M., Barla, M., Turinetti, G., & Amann, F. (2017). A multi-stage triaxial testing procedure for low permeable geomaterials applied to Opalinus Clay. *Journal of Rock Mechanics and Geotechnical Engineering*, *9*(3), 519-530.
https://doi.org/https://doi.org/10.1016/j.jrmge.2017.04.003

Wissa, A. E. Z. (1969). Pore Pressure Measurement in Saturated Stiff Soils. *95*(4), 1063-1073.
https://doi.org/doi:10.1061/JSFEAQ.0001304

Zoback, M. D., & Zinke, J. C. (2002). Production-induced Normal Faulting in the Valhall and Ekofisk Oil Fields. *pure and applied geophysics*, *159*(1), 403-420.
https://doi.org/10.1007/PL00001258

Aadnoy, B. S. (1991). Effects of reservoir depletion on borehole stability. *Journal of petroleum science & engineering*, *6*(1), 57-61. https://doi.org/10.1016/0920-4105(91)90024-H

Acknowledgments

This publication has been produced with support from the Research Council of Norway (RCN) through the NCCS Centre (RCN# 257579), performed under the Norwegian research programme Centres for Environment-friendly Energy Research (FME). The authors would like to thank the partners in PL360 with funding from CLIMIT (Project 223122) and Statoil (Equinor) for the core material used in this study. Thanks also to Bjørnar Slensvik and Halvard Smith for help with sample preparation and discussions on testing protocols.

Open Research

All experimental data used from triaxial testing herein is published at DataverseNO (Magnus Soldal, 2022, "Replication Data for: Experimental evaluation of predicted undrained pore pressure generation as function of stress path and orientation in the Draupne shale").